08

Influence of Electronic Structure on the Topography of Ge(100) and Si(100) Surfaces in Scanning Tunneling Microscopy

© V.E. Remele, M.V. Kuzmin

Ioffe Institute,
St. Petersburg, Russia

E-mail: m.kuzmin@mail.ioffe.ru

Received September 2, 2025
Revised January 16, 2026
Accepted January 22, 2026

The analysis of scanning tunneling microscopy images for $c(4 \times 2)$ and $p(2 \times 2)$ reconstructions on the (100) face of germanium and silicon, which are simulated using the density functional theory and measured at 12 K, has been performed. It is shown that depending on the sign and magnitude of the bias voltage, the appearance of these images can be significantly transformed, and the observed topographic relief can to a greater extent reflect the atomic geometry or electronic structure features of the surface. The obtained results demonstrate that when interpreting scanning tunneling microscopy data for these reconstructions, it is necessary to carefully consider a number of factors, including detailed knowledge of the local density of states.

Keywords: Surface reconstruction, atomic structure, electronic properties, density functional theory.

DOI: 10.61011/PSS.2026.01.63248.243-25

1. Introduction

The surfaces of semiconductor crystals are subject to structural and electronic rearrangement, resulting in „two-dimensional" (surface) reconstructions with unique physicochemical properties [1,2]. Scanning tunneling microscopy (STM) is one of the most informative methods for studying them on a subnanometer scale. However, the interpretation of STM results may be non-trivial for a number of reasons. For example, in the case when the characteristic time of elementary processes on the surface (vibrational movements of atoms and molecules, diffusion of impurities, fluctuations of steps, etc.) is much shorter than the time of movement of the STM tip, the observed topography will represent an average pattern, and not a „snapshot" of the surface structure. Thus, surface dimers on the edge (100) of silicon and germanium at room temperature due to their rapid fluctuations between two possible asymmetric (tilted) configurations $Si^{\uparrow}-Si_{\downarrow}$ ($Ge^{\uparrow}-Ge_{\downarrow}$) and $Si^{\downarrow}-Si_{\uparrow}$ ($Ge^{\downarrow}-Ge_{\uparrow}$), or flip-flop motion, are displayed on STM images in a symmetrical form [3,4]. At the same time, such fluctuations can be „frozen" at a low temperature ($T < 200$ K), and then the surface dimers are visualized as asymmetric.

Another well-known problem that makes it difficult to interpret STM images is related to the influence of the electronic structure. For the already mentioned Si(100) and Ge(100) faces, the relief observed in the STM is determined to a greater extent by the spatial distribution of the local density of states (LDoS) on the surface, rather than by its atomic geometry. In other words, the type of STM images strongly depends on the bias voltage (V), and when this parameter is varied, various electronic states on the surface can contribute to the observed image. The nature of these states, however, is still a matter of debate even for such well-studied systems as Si(100) and Ge(100) [5–29]. It was shown in Refs. [5,6] that for small values of $|V|$, the STM topography of the Si(100) surface is determined by π- or π^*-states (depending on the sign of the applied bias voltage) located on the energy scale, respectively, slightly below the maximum of the valence band and slightly above the minimum of the conduction band on the surface, and that at higher values of $|V|$, the main contribution to the STM image is made by other states other than π and π^*-states. As for the latter, there is no unambiguous explanation in the literature: in various studies they have been identified as σ^*-states caused by bonds between atoms in dimers [6–8], and states caused by the inverse π^*-back bonding of the upper dimer atoms [6,9] or surface resonances [10].

In the case of the Ge(100) surface, the vertex of the valence band has a more complex character than for Si(100), and is determined not only by π-states [11–15]. It was shown in Ref. [16] that STM images of this surface obtained in the filled state mode in the range of values V from -0.6 to -0.1 V, very strongly depend on the bias voltage. For -0.1 V features in the image were attributed to the inverse π bonds of dimer atoms, and in the range from -0.6 to 0.45 V — π-states caused by dangling bonds of these atoms. This interpretation was questioned in the message [17]. Its authors concluded that the vertex of the valence band of the Ge(100) surface is determined by the state caused by the volumetric lattice of germanium, which is confirmed by other studies [14,15]. A similar, no less complicated situation is observed for the electronic structure of the Ge(100) surface above the Fermi level [18–27]. A brief overview of the surface states capable of contributing

to Si(100) and Ge(100) STM images at various values of V can be found in Ref. [29]. Thus, in order to reliably identify the electronic states responsible for the STM topography of the surfaces under consideration, further systematic theoretical and experimental studies are needed. Obviously, such studies are important for understanding the results of STM not only of pure silicon and germanium surfaces, but also of adsorbates [30–32] and impurities [33,34] on these substrates.

In this paper, a comparative theoretical and experimental study of STM images of $c(4 \times 2)$ and $p(2 \times 2)$ reconstructions on Ge(100) and Si(100) surfaces has been carried out to clarify the main patterns of influence of the electronic structure on them and to clarify the unresolved issues listed above (at least partially). The calculations were performed on the basis of density functional theory (DFT). For a correct comparison of the obtained results with the experimental data, the latter were performed at $T = 12$ K.

2. Calculation method

The calculations were performed in the Quantum Espresso [35] software package within the generalized gradient approximation (GGA) using the exchange-correlation functional PBE [36] and ultra-soft pseudopotentials [37]. When performing the calculations, the basis of plane waves with cutoff energies in terms of the wave function and electron density equal to 46 and 221 Ry for Si and 46 and 239 Ry for Ge, respectively, was used. The integration in the Brillouin zone was performed with the density of the grid of the quasi-wave vector of the inverse space $2 \times 4 \times 1$ for Si and $3 \times 6 \times 1$ for Ge. When calculating the density of states, the density of the grid was increased by 4 times for each case. To simulate the surface, a lattice cell containing a slab (slab) with a thickness of five monoatomic layers and a vacuum gap of 15 Å was used. The lower part of the plate was passivated with hydrogen atoms to eliminate broken bonds. The reconstructions considered in this paper were obtained by geometric optimization of the atomic structure performed using the Broyden-Fletcher-Goldfarb-Shano (BFGS) [38] algorithm. At the same time, the two lower layers of the plate were fixed, and the position of the atoms in the three upper layers varied. For the structures obtained during geometric optimization, STM images were modeled using the Tersoff-Hamann [39] approach using the critic2 software package [40,41].

3. Experimental procedure

The experiments were carried out *in situ* using a Scienta Omicron Fermi SPM scanning tunneling microscope (Germany) at a residual pressure of $< 1 \cdot 10^{-10}$ mbar. When registering STM images, the temperature of the sample, as indicated in sec. 1, was maintained equal to 12 K, and the temperature of the microscope scanner — equal to 20 K.

Parameters of optimized structures $c(4 \times 2)$ and $p(2 \times 2)$. Designations: d is the distance between atoms (bond length) in the dimer and α is the angle of inclination of the dimer relative to the surface

	Si(100)		Ge(100)	
	d, Å	α, deg	d, Å	α, deg
$c(4 \times 2)$	2.37	19.26	2.58	17.23
$p(2 \times 2)$	2.37	19.22	2.58	20.11

The images were obtained in direct current mode. The STM tips were made of tungsten. The WSXM software package was used for post-processing and image analysis [42].

Single crystals of Ge(100) doped with Sb (n-type, $\sim 1 \cdot 10^{19}$ cm^{-3}) were used as samples. To prepare a clean surface, a series of ion bombardments Ar^+ with an energy of 1.0 keV at 673 K was used, alternating with heating of the crystal at 900 K. The procedure was repeated until an atomically smooth surface reconstruction was obtained, free of foreign impurities.

4. Results and their discussion

4.1. Atomic geometry

Figure 1 shows optimized atomic structures of the $c(4 \times 2)$ and $p(2 \times 2)$ reconstructions on Si and Ge surfaces. The long-range order and type of the lattice cell in them are determined by the features of dimerization in the upper atomic layer of the crystal. The inclination of dimers ($\uparrow - \downarrow$ or $\downarrow - \uparrow$) alternates in two directions in the structure $c(4 \times 2)$ (Figure 1, a): along the rows they form and in the transverse direction perpendicular these rows. In other words, the nearest neighbors for the $Si^{\uparrow}{-}Si_{\downarrow}$ ($Ge_{\uparrow}{-}Ge^{\downarrow}$) dimer in a row and in adjacent rows will be the dimers $Si_{\downarrow}{-}Si^{\uparrow}$ ($Ge_{\downarrow}{-}Ge^{\uparrow}$) and vice versa. Thus, the slope of dimers in the reconstruction $c(4 \times 2)$ is similar to the direction of electron spin in antiferromagnetic systems. In the structure $p(2 \times 2)$ (Figure 1, b), the alternation of asymmetric dimers occurs only in one direction — along their rows. In the transverse direction, neighboring dimers are always tilted in the same direction. The values of the bond length and the angle of inclination of the dimers in the obtained structures are shown in the table.

These values are in good agreement with the previously published values [43–48]. In terms of energy, the reconstructions under consideration differ very slightly, i. e. they are practically degenerate; for example, for silicon, such a difference is 0.7 meV/dimer [49]. This leads to the fact that when interacting with the needle, the structure $c(4 \times 2)$, which is the ground state, can spontaneously transition to $p(2 \times 2)$ and vice versa. Such transitions will be discussed in more detail in sec. 4.3.2.

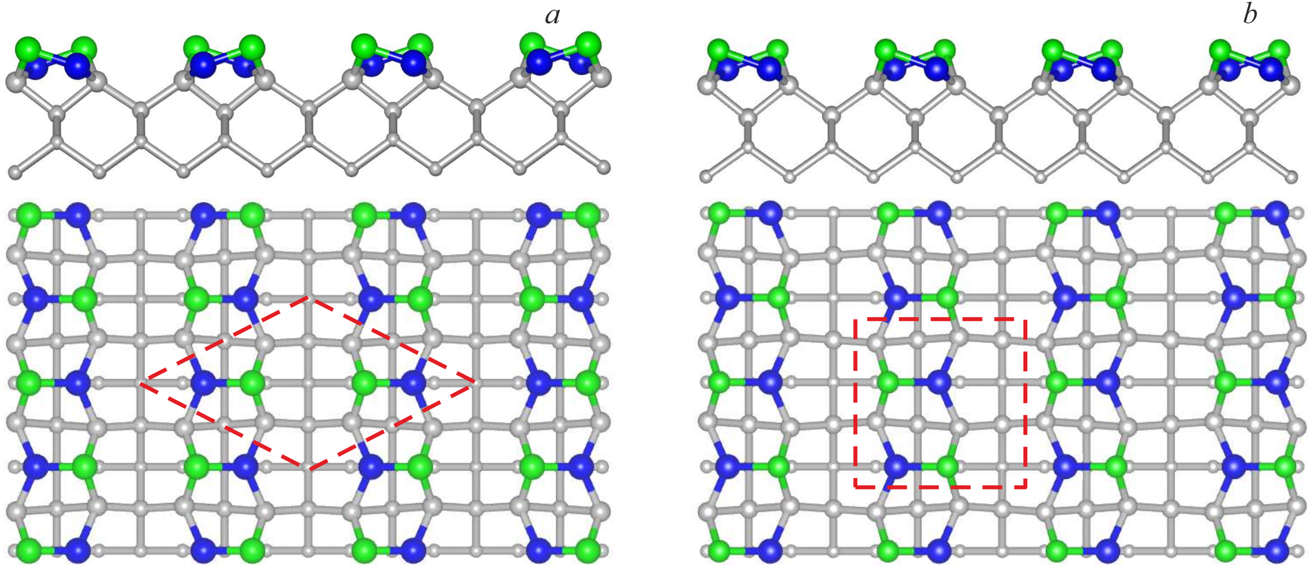

Figure 1. Atomic models of Si(100) and Ge(100) reconstructions: a — $c(4 \times 2)$, b — $p(2 \times 2)$. The upper part of each panel shows a side view of the atomic structure, and the lower part shows a top view. The dotted line marks the boundaries of the elementary cell of the surface superstructure.

Next, the reconstructions $c(4 \times 2)$ and $p(2 \times 2)$ shown in Figure 1 will be used to calculate the density of states and model STM images.

4.2. Electronic structure

Figures 2 and 3 show the results of calculating the partial density of states (pDoS), i. e. projections of the total density of states onto the s and p orbitals of dimer atoms (solid lines), for reconstructions $c(4 \times 2)$ and $p(2 \times 2)$ on Si and Ge. The area shaded in gray shows the total density of states for the upper ($Si^{\uparrow}$ or $Ge^{\uparrow}$) and lower ($Si_{\downarrow}$ or $Ge_{\downarrow}$) atoms. The value $E = 0$ on the energy scale corresponds to the position of the Fermi level.

Let us highlight the most characteristic features of these results.

First of all, when analyzing the obtained pDoS distributions, it is necessary to take into account that in dimers on the surfaces of Si(100) and Ge(100), π bonds are formed and charge flows from the lower atom to the upper atom. This should lead to the appearance of bonding π- and anti-bonding π^*-states below and above the Fermi level, respectively. For all reconstructions in Figures 2 and 3, two characteristic narrow bands associated with π^*-states are observed in the energy range above the Fermi level: one at low values of E (~ 0.1 eV), and the other is observed at higher values: $\sim 0.8-0.9$ eV for Si (Figure 2) and $\sim 0.6-0.8$ eV for Ge (Figure 3). The main contribution to these bands is provided by the anti-bonding p_z-orbital (the axis z is oriented normal to the surface). At $E \approx 0.1$ eV, this orbital is localized near the lower dimer atom. At higher energy values, it is less localized, especially for Si: the corresponding density of states is distributed near both dimer atoms. In addition, a small addition to it is provided by the p_x orbital located at the lower atom (the axis x lies in the surface plane and is perpendicular to the rows of dimers).

At higher energy values (≥ 1.2 eV for Ge and ≥ 1.4 eV for Si), several anti-bonding orbitals simultaneously contribute to the density of states, including s and p_y (the axis y is parallel to the rows of dimers). This is caused by the formation of σ- and/or reverse π-bonds between surface atoms.

Below the Fermi level, the contribution of the bonding p_z-orbital to the density of states is dominant at energies from -0.9 to -0.25 eV for Si and from -1.1 to -0.5 eV for Ge. This orbital is localized on the upper atoms of the dimers. At lower energies, the density of states is determined by several, less localized, orbitals, and their contributions are comparable to them.

We also note another interesting detail of the electronic structure of the reconstructions under consideration. The peak of the valence band for Si and Ge is determined by different states. In the Si case, the maximum of this band (it is below the Fermi level at $\sim 0.23-0.25$ eV in Figure 2) is formed primarily by the p_z-orbital, to which s-states are added. A fundamentally different pattern is observed for Ge reconstructions. In this case, the maximum of the valence band ($\sim 0.05-0.08$ eV is below the Fermi level in Figure 3) is caused by the orbital p_y. As for the minimum of the conduction band, its nature is the same for all the studied structures. The anti-bonding p_z-states are responsible for its formation.

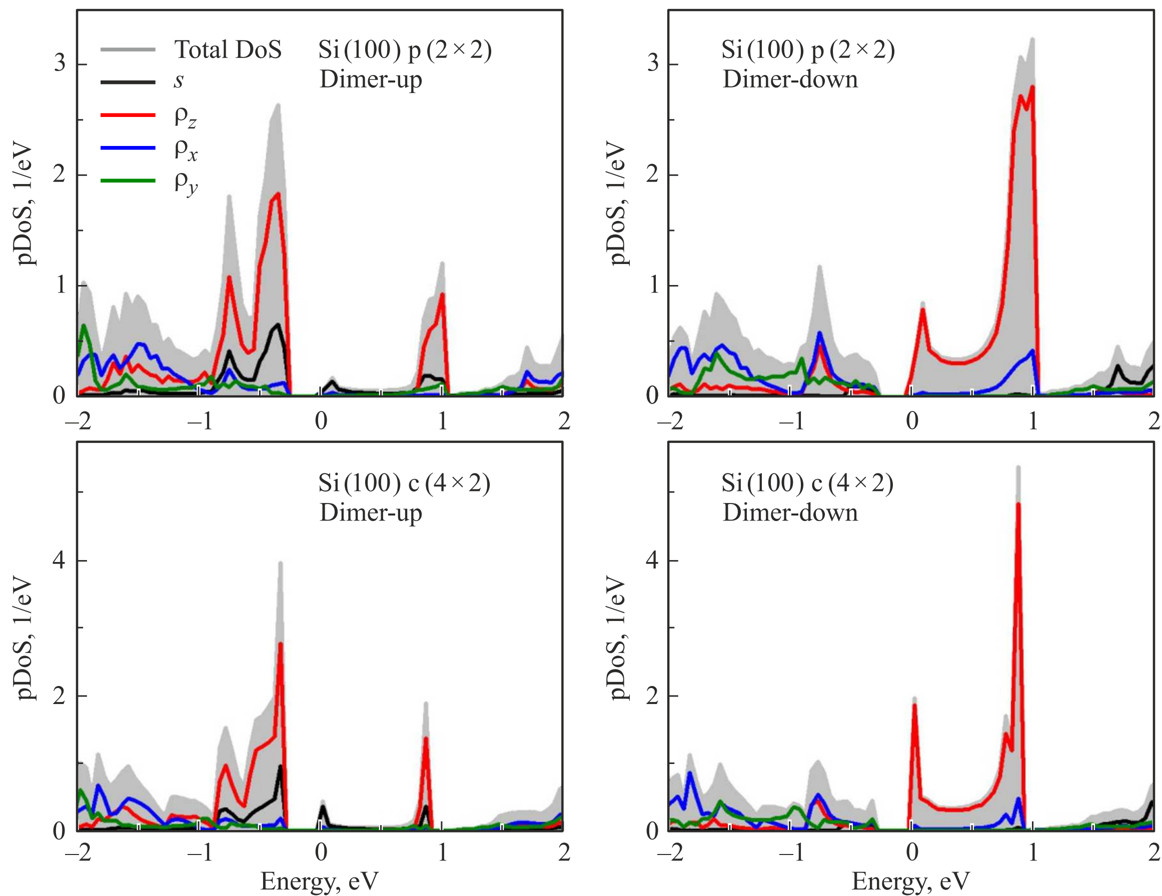

Figure 2. Partial density of states for reconstructions on the Si(100) surface.

4.3. Scanning tunneling microscopy

4.3.1. Modeling

When analyzing the STM results, it is important to take into account that the contribution of the surface state with energy E to the tunneling current depends on the applied bias voltage V. According to Refs. [41,50], tunneling current can be represented as $I \propto \int_0^{eV} \rho(E)T(E, eV)dE$, where e is the electron charge, $T(E, eV)$ — the permeability of the barrier between the tip and the sample for the electron (i.e., the probability of the latter passing through the vacuum gap), and $\rho(E)$ — the LDoS value on the sample surface. This expression is valid when the LDoS of the tip surface near the Fermi level is weakly dependent on energy, which is a reasonable assumption in the case of metal needles made, in particular, of tungsten. The barrier permeability value can be expressed as $T(E, eV) = e^{-2\kappa s}$, where s is the length of the vacuum gap, and κ is the inverse attenuation length. The last value is

$$\kappa = \sqrt{\frac{2m}{\hbar^2}\left(\frac{\varphi + \varphi^*}{2} - E + \frac{eV}{2}\right) + k_\parallel^2},$$

where φ and φ^* is the values of the output of the sample and needle, respectively, $k_\parallel$ is the component of the wave vector for the surface state parallel to the surface, m is the mass of an electron and $\hbar$ is the Planck-Dirac constant. It follows from the expressions just given that the contribution to the tunneling current of a state with an energy of E is maximal at $V = E/e$ and decreases with increasing bias voltage.

Figure 4 shows the simulation results of STM images for reconstructions $c(4 \times 2)$ and $p(2 \times 2)$ at different values of the bias voltage. The geometric positions of the upper and lower dimer atoms are shown by green and blue circles, respectively. As can be seen, the characteristic features observed for the two structures are similar, and the differences in the STM images are due to the unequal arrangement of atoms on these surfaces. Therefore, further in this section we will consider only the results for reconstruction $p(2 \times 2)$. The conclusions drawn for this structure can easily be transferred to the case of reconstruction $c(4 \times 2)$.

First of all, we note that the sign of the bias voltage in Figure 4 has a qualitative effect on the main trends in image changes with increasing parameter V. A simpler case is the tunneling of electrons from the filled states of the sample to empty levels in the needle (case $V < 0$). In this mode, as follows from the figure, the upper dimer atoms correspond to the projections in the images, i.e. the areas where the needle rises to the maximum height. This is due to two

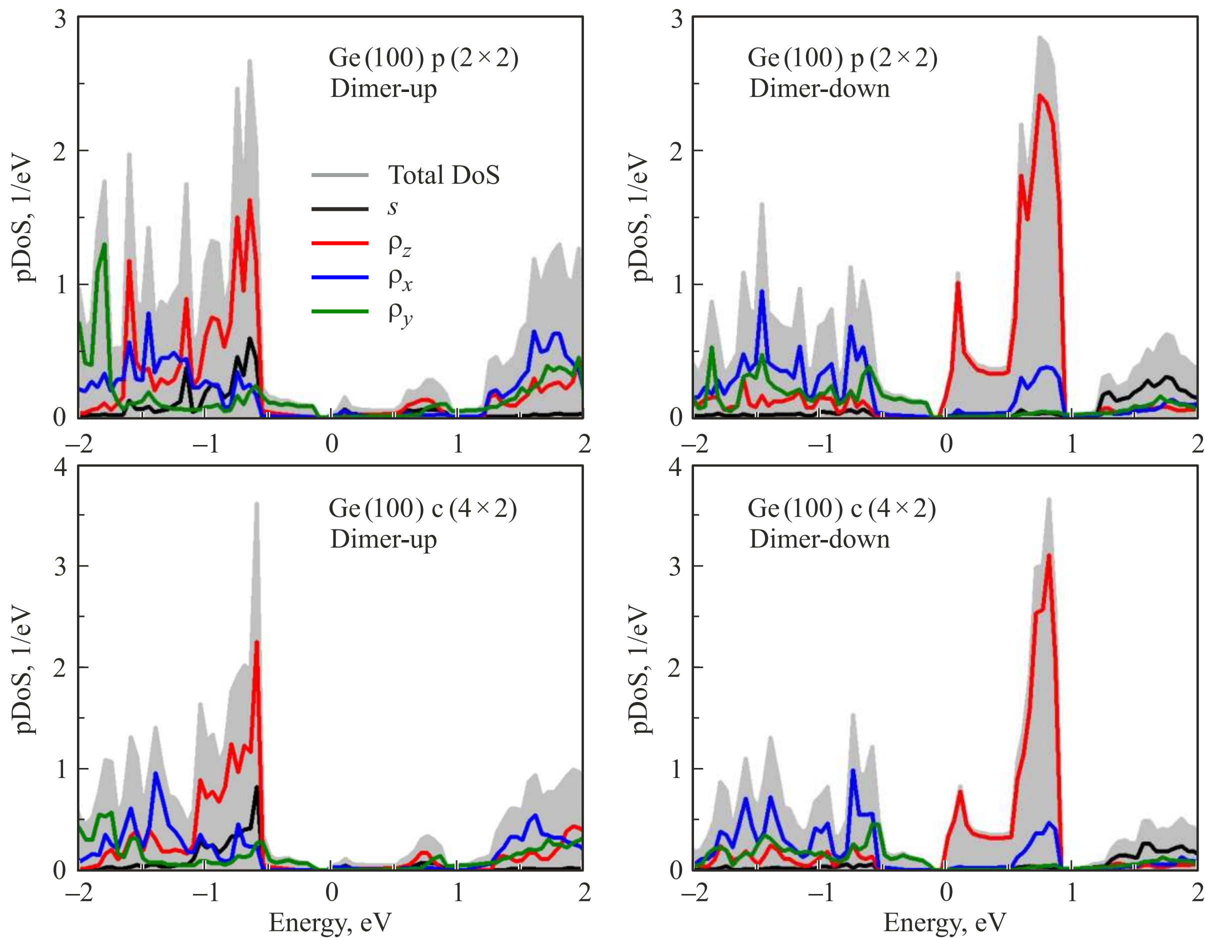

Figure 3. The same as in Figure 2, but for the Ge(100) surface.

factors. Firstly, the LDoS near these atoms is higher than at the lower atoms of the dimers. And secondly, the atoms $Si^{\uparrow}$ and $Ge^{\uparrow}$ are elevated above the atoms $Si_{\downarrow}$ and $Ge_{\downarrow}$ by 0.75–0.88 Å.

It should also be noted that in the case of Ge, the protrusions are well resolved for all values of V from -2.0 to -0.5 V. It can be assumed that this is due to the shape of the p_z orbitals localized on the atoms of $Ge^{\uparrow}$. A similar trend is observed for Si at biases of V from -1.5 to -0.5 V. In the case of $V = -2.0$ V protrusions do not resolve and merge into a zigzag chain. This is because the tunneling current at a given bias voltage is approximately equally driven by multiple orbitals. Thus, in the filled state mode, for all selected values of V, the protrusions in the obtained images correspond to the positions of the $Ge^{\uparrow}$ and $Si^{\uparrow}$ atoms. As already mentioned, this case is easy to interpret: the observed topographic relief on the STM images roughly repeats the atomic structure of the surface.

A more complicated situation is observed in the empty states mode ($V > 0$). For small values of displacement stresses (0.5 V) in the case of Ge, the protrusions in the STM images correspond to the lower atoms of the dimers. These features form zigzag chains. At the same time, depressions are observed in the images near the upper atoms. This topography is due to the fact that π^* states in the energy range ≤ 0.5 eV are strongly localized on Ge $\text{atoms}_{\downarrow}$ (Figures 2 and 3).

For Si in the image at $V = 0.5$ V, similar zigzag chains are also observed due to the atoms of $Si_{\downarrow}$. In addition, small rounded protrusions are visible, which are located near $Si^{\uparrow}$ atoms and are absent in the case of Ge. Apparently, such additional features are due to the contribution of s-orbitals localized on $Si^{\uparrow}$ atoms to the tunneling current (Figure 2).

When the bias voltage is increased to 1.0 V, both the lower and upper atoms of germanium and silicon dimers make a comparable contribution to STM images, which leads to the appearance of wide bands instead of zigzag chains. The reason for this is the less localized nature of π^*-states at energies ~ 1.0 eV (sec. 4.2). This effect is more pronounced in the case of silicon reconstructions, for which dimers have a shape resembling a symmetrical one. Obviously, in this case, the higher density of states on the lower atom of the dimer is compensated by the geometric position of the upper atom — it is elevated above the lower one. Similar conclusions can be drawn for the case of $V = 1.5$ V.

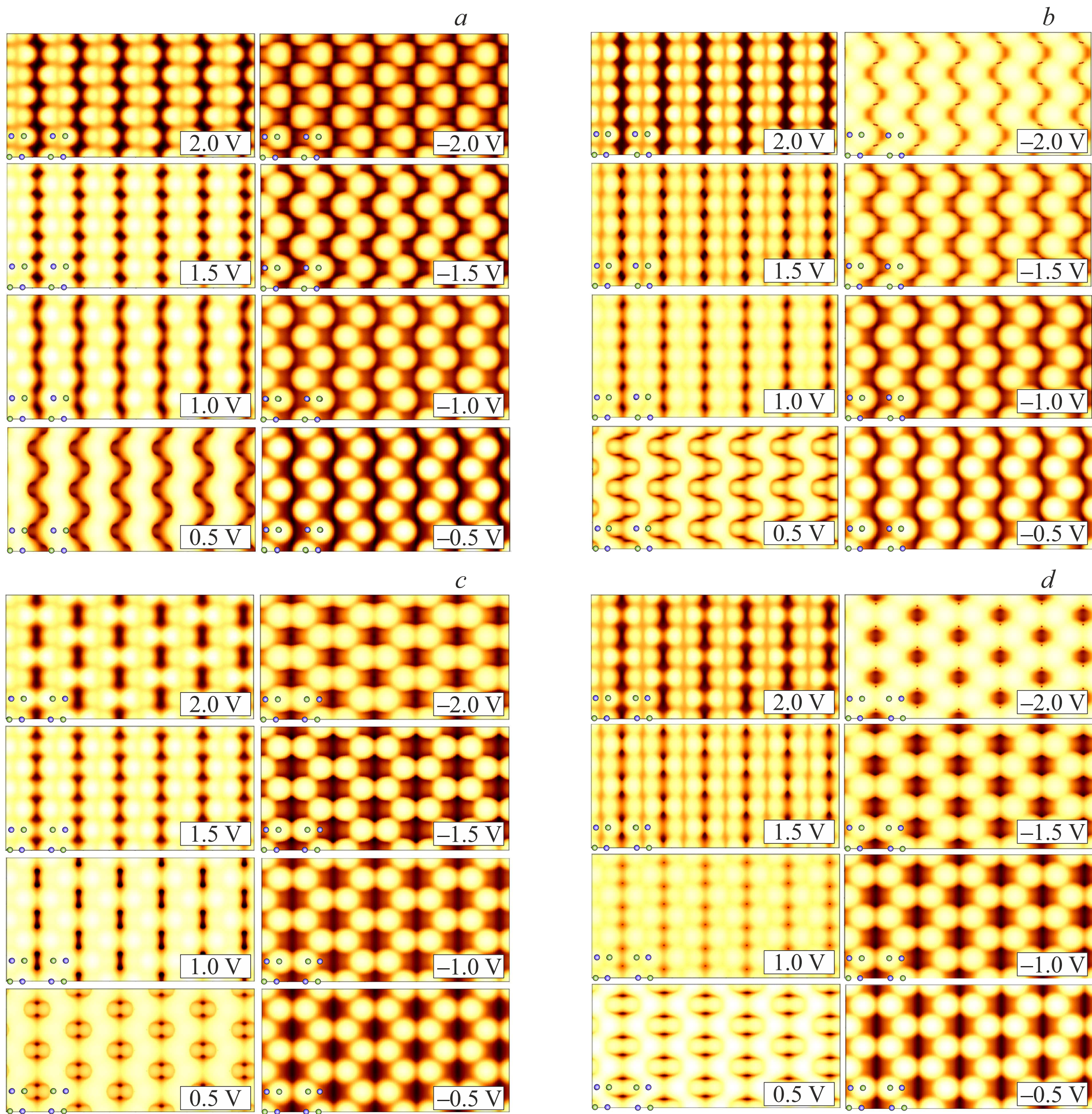

Figure 4. STM images modeled for various reconstructions: a — Ge(100)$p(2\times2)$, b — Si(100)$p(2\times2)$, c — Ge(100)$c(4\times2)$, d — Si(100)$c(4\times2)$. The values of the displacement stresses are indicated on the inserts. The green and blue circles indicate the positions of the upper and lower dimer atoms.

The pattern qualitatively changes at $V = 2.0$ V. The most striking features (protrusions) in the image correspond to the upper atoms of the dimers. This is more pronounced in the case of Ge. The lower atoms of the dimers also have characteristic features. Their brightness is slightly lower than in the case of the upper atoms. This transformation of STM images is due to the pDoS changes described in section 4.2.

Thus, the appearance of the images obtained for $V > 0$ is qualitatively different from those for $V < 0$, and also significantly depends on the magnitude of the bias voltage. At low values of V, the main features of images in the empty state mode are due to the lower dimer atoms and form continuous zigzag chains. The upper dimer atoms make a small contribution to the images (for Si) or not at all (for Ge). At high values of V, the main features of the images are related to the upper atoms. In the intermediate range of bias voltage values, both dimer atoms make approximately the same contribution to the tunneling current, which leads to the appearance of stripes in the image. Such a complex dependence of the STM topography

on the electronic structure means that the filled state mode is more suitable for direct visualization of the atomic structure of Si(100) and Ge(100) reconstructions; at the same time, in the empty state mode, the observed relief is primarily due to the peculiarities of the electronic structure of these surfaces.

4.3.2. Experiment

As is known, the use of the exchange-correlation functional of PBE in calculations of the electronic structure leads to a systematic underestimation of the band gap [51]. Therefore, the comparison of STM images obtained using this functional with experimental images at the same values of the bias voltage is, strictly speaking, incorrect. In this paper, the aim of the experiment was to identify general trends in the evolution of STM images with variations in bias voltage and compare them with similar patterns observed in modeling (sec. 4.3.1). The measurements were carried out only for reconstructions on the surface of Ge(100). A reversible phase transition $c(4 \times 2) \leftrightarrow p(2 \times 2)$ is possible during the interaction of this surface with the STM tip, as reported in Refs. [20,21]. According to these studies, the direction of the arrow in the designation of this transition depends on the type of carriers injected into the crystal surface from the needle. When tunneling electrons into the empty states of the $c(4 \times 2)$ structure it switches to $p(2 \times 2)$ and then persists until the bias voltage polarity is switched V. After switching the polarity and tunneling electrons from the filled states $p(2 \times 2)$ into the needle, i. e. injection of holes into the crystal, the specified structure again passes into $c(4 \times 2)$ and remains unchanged until the sign of the bias voltage and the type of carriers injected into the sample change. The above scheme of phase transformations is fully confirmed in the present study. These results mean that the analysis of STM images of the structure $c(4 \times 2)$ can be carried out only for the case $V < 0$, and the structure $p(2 \times 2)$ can be analyzed only for the case $V > 0$.

Figure 5 shows experimental STM images obtained at values $V = -0.6$ and -2.0 V. As can be seen, the topography of the reconstruction $c(4 \times 2)$ in these images is almost unchanged, which is in good agreement with the calculation results (Figure 4). The twin protrusions in Figure 5 are caused by pairs of neighboring $Ge^{\uparrow}$ atoms in the structure $c(4 \times 2)$, as in the case in Figure 4. The only difference is that in the patterns obtained in the experiment, these atoms are not resolved. One of the possible reasons for this difference may be the imperfect shape of the needle used in the measurements. In addition, sideways tunneling [29] may play a significant role in the experiment, which is not taken into account when modeling STM images. It can be assumed that when registering the patterns in Figure 5, the needle occupies the maximum height when it is located between neighboring $Ge^{\uparrow}$ atoms and tunneling occurs from them simultaneously. The line

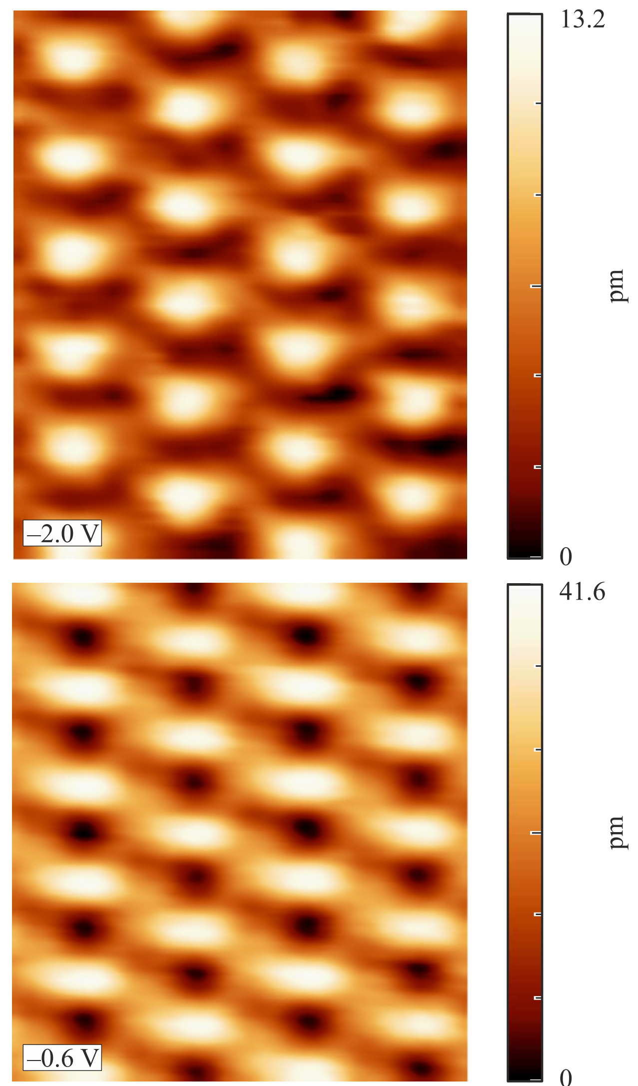

Figure 5. STM images of the Ge(100)$c(4 \times 2)$ surface, obtained with $V = -0.6$ and -2.0 V. Tunneling current 2.0 nA. The size of the images is 3.7×4.1 and 3.7×4.5 nm, respectively.

profiles obtained for the protrusions in Figure 5 (not shown in the article) fully confirm this assumption.

It should be noted also that the contrast value in the images in Figure 5 depends on the voltage value V. The height difference is 41.6 pm at -0.6 V, and 13.2 pm at -2.0 V. The reason why the contrast in the images changes is easy to understand by comparing the densities of states on $Ge^{\uparrow}$ and $Ge^{\downarrow}$ atoms in the reconstruction of $c(4 \times 2)$ at the corresponding energies in Figure 3.

In the empty state mode at low values of the bias voltage ($V = 0.3$ V), the protrusions in the experimental image (Figure 6) correspond to the $Ge^{\downarrow}$ atoms of reconstruction $p(2 \times 2)$. These protrusions form zigzag lines, which is in full agreement with the calculated data in Figure 4.

When the value V is increased to 0.8 V, the zigzag chains in the image of the structure $p(2 \times 2)$ smoothly

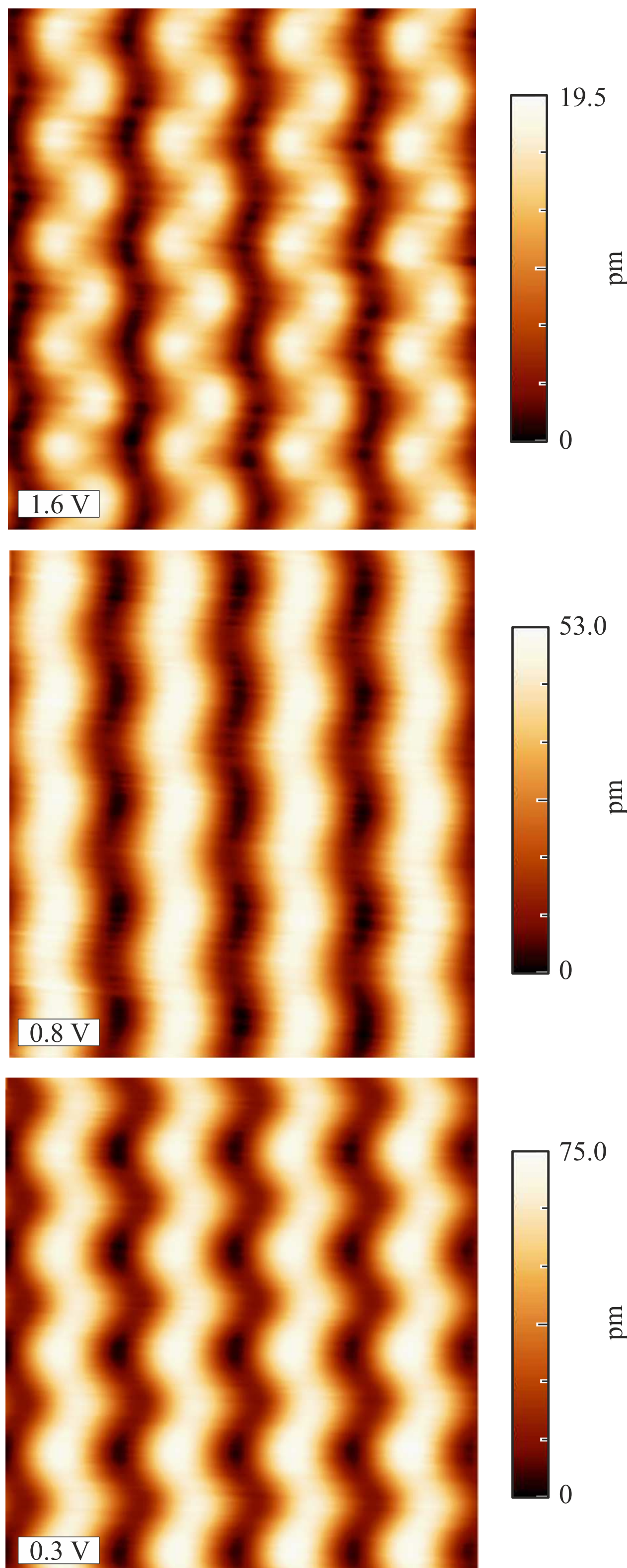

Figure 6. STM images of the Ge(100)$p(2 \times 2)$ surface, obtained with $V = 0.3$, 0.8 and 1.6 V. Tunneling current 500 pA. The size of the images is 3.7×3.9, 3.5×3.8 and 3.7×4.1 nm, respectively.

transform into almost straight lines (stripes). This is due to the increased contribution of $Ge^{\uparrow}$ atoms to the tunneling current. Finally, at 1.6 V, the characteristic zigzag chains reappear in the image. The maxima of the tunneling current under these conditions correspond to $Ge^{\uparrow}$ atoms. All these transformations of STM images are consistent with the results of DFT (Figure 4).

Noteworthy is the consistent decrease in image contrast with increasing bias voltage in Figure 6: the height difference at $V = 0.3$, 0.8 and 1.6 V is 75.0, 53.0 and 17.5 pm, respectively. The reasons for this are similar to the reasons for changing the contrast of STM images at $V < 0$, discussed above.

Thus, the experiments carried out fully confirm the basic patterns that were revealed for the STM images obtained for the Ge(100) surface using DFT (Figures 3 and 4).

5. Conclusion

Using DFT modeling and measurements at 12 K, the general patterns of the effect of the electronic structure of reconstructions $c(4 \times 2)$ and $p(2 \times 2)$ on Ge(100) and Si(100) on the appearance of STM images of these surfaces in the mode of constant tunneling current are investigated. It is shown that the topographic relief on them significantly depends on the displacement stress. At $V < 0$, i.e. in the filled state mode, STM images are determined primarily by the atomic structure of surfaces at all displacement stresses from -2.0 to -0.5 V. The protrusions in these patterns correspond to dimeric $Ge^{\uparrow}$ and $Si^{\uparrow}$ atoms, in particular, they are caused by tunneling from orbitals localized on these p_z atoms. At $V > 0$ (empty state mode) the situation is changing dramatically: The STM images reflect to a large extent the electronic rather than the atomic structure of the reconstructions. At low values of $V \approx 0.3-0.5$ V, the main protrusions on them correspond to the lower atoms of the dimers, forming zigzag chains, and are caused by antibonding π^* states strongly localized on these atoms. As the bias voltage increases to $0.8-1.0$ V, these states become less localized, and both dimer atoms make approximately equal contributions to the images, leading to the appearance of streaks. With a further increase in voltage (at $V > 1.5$ V), the main features in the STM images correspond to the upper atoms of the dimers, and the tunneling current is determined by different orbitals on the surface.

Conflict of interest

The authors declare that they have no conflict of interest.

References

[1] W. Mönch. Semiconductor Surfaces and Interfaces. In: Springer Series in Surface Surfaces, v. 26. Springer-Verlag, Berlin–Heidelberg (2001). 548 p.

[2] P. Laukkanen, M. Punkkinen, M. Kuzmin, K. Kokko, X. Liu, B. Radfar, V. Vähänissi, H. Savin, A. Tukiainen, T. Hakkarainen, J. Viheriälä, M. Guina. Rep. Prog. Phys. **87**, *4*, 044501 (2024).
[3] R.J. Hamers, R.M. Tromp, J.E. Demuth. Phys. Rev. B **34**, *8*, 5343 (1986).
[4] R.A. Wolkow. Phys. Rev. Lett. **68**, *17*, 2636 (1992).
[5] X.R. Qin, M.G. Lagally. Phys. Rev. B **59**, *11*, 7293 (1999).
[6] K. Hata, S. Yasuda, H. Shigekawa. Phys. Rev. B **60**, *11*, 8164 (1999).
[7] H. Okada, Y. Fujimoto, K. Endo, K. Hirose, Y. Mori. Phys. Rev. B **63**, *19*, 195324 (2001).
[8] K.S. Nakayama, M.M.G. Alemany, T. Sugano, K. Ohmori, H. Kwak, J.R. Chelikowsky, J.H. Weaver. Phys. Rev. B **73**, *3*, 035330 (2006).
[9] L. Perdigão, D. Deresmes, B. Grandidier, M. Dubois, C. Delerue, G. Allan, D. Stiévenard. Phys. Rev. Lett. **92**, *21*, 216101 (2004).
[10] K. Hata, S. Yoshida, H. Shigekawa. Phys. Rev. Lett. **89**, *28*, 286104 (2002).
[11] A. Dimoulas, P. Tsipas, A. Sotiropoulos, E.K. Evangelou. Appl. Phys. Lett. **89**, *25*, 252110 (2006).
[12] T. Nishimura, K. Kita, A. Toriumi. Appl. Phys. Lett. **91**, *12*, 123123 (2007).
[13] P. Tsipas, A. Dimoulas. Appl. Phys. Lett. **94**, *1*, 012114 (2009).
[14] M. Kuzmin, P. Laukkanen, J. Mäkelä, M. Tuominen, M. Yasir, J. Dahl, M.P.J. Punkkinen, K. Kokko. Phys. Rev. B **94**, *3*, 035421 (2016).
[15] H. Seo, R.C. Hatch, P. Ponath, M. Choi, A.B. Posadas, A.A. Demkov. Phys. Rev. B **89**, *11*, 115318 (2014).
[16] M.W. Radny, G.A. Shah, S.R. Schofield, P.V. Smith, N.J. Curson. Phys. Rev. Lett. **100**, *24*, 246807 (2008).
[17] B. Yan, C. Yam, A.L. da Rosa, T. Frauenheim. Phys. Rev. Lett. **103**, *18*, 189701 (2009).
[18] O. Gurlu, H.J.W. Zandvliet, B. Poelsema. Phys. Rev. Lett. **93**, *6*, 066101 (2004).
[19] J.A. Kubby, J.E. Griffith, R.S. Becker, J.S. Vickers. Phys. Rev. B **36**, *11*, 6079 (1987).
[20] Y. Takagi, K. Nakatsuji, Y. Yoshimoto, F. Komori. Phys. Rev. B **75**, *11*, 115304 (2007).
[21] Y. Takagi, Y. Yoshimoto, K. Nakatsuji, F. Komori. Surf. Sci. **559**, *1*, 1 (2004).
[22] U. Schwingenschlögl, C. Schuster. Chem. Phys. Lett. **449**, *1−3*, 126 (2007).
[23] K. Tomatsu, K. Nakatsuji, M. Yamada, F. Komori. Phys. Rev. Lett. **103**, *26*, 266102 (2009).
[24] L. Kipp, R. Manzke, M. Skibowski. Surf. Sci. **269−270**, 854 (1992).
[25] M. Skibowski, L. Kipp. J. Electron Spectrosc. Relat. Phenom. **68**, 77 (1994).
[26] C. Jeon, C.C. Hwang, T.-H. Kang, K.-J. Kim, B. Kim, Y. Chung, C.Y. Park. Phys. Rev B **74**, *12*, 125407 (2006).
[27] P.E.J. Eriksson, M. Adell, K. Sakamoto, R.I.G. Uhrberg. Phys. Rev. B **77**, *8*, 085406 (2008).
[28] X.-Y. Ren, H.-J. Kim, C.-Y. Niu, Y. Jia, J.-H. Cho. Sci. Rep. **6**, 27868 (2016).
[29] M. Kuzmin, J. Mäkelä, J.-P. Lehtiö, M. Yasir, M. Tuominen, Z.S.J. Rad, A. Lahti, M.P.J. Punkkinen, P. Laukkanen, K. Kokko. Phys. Rev. B **98**, *15*, 155322 (2018).
[30] J. Tonhäuser, N. Kubetschek, U. Kürpick, R. Matzdorf. Phys. Rev. B **106**, *11*, 115404 (2022).
[31] E.V.S. Hofmann, E. Scalise, F. Montalenti, T.J.Z. Stock, S.R. Schofield, G. Capellini, L. Miglio, N.J. Curson, W.M. Klesse. Appl. Surf. Sci. **561**, 149961 (2021).
[32] W. Koczorowski, T. Grzela, M.W. Radny, S.R. Schofield, G. Capellini, R. Czajka, T. Schroeder, N.J. Curson. Nanotechnol. **26**, *15*, 155701 (2015).
[33] K. Noatschk, E.V.S. Hofmann, J. Dabrowski, N.J. Curson, T. Schroeder, W.M. Klesse, G. Seibold. Surf. Sci. **713**, 121912 (2021).
[34] P.T. Różański, G.W. Bryant, M. Zieliński. Sci. Rep. **14**, 18062 (2024).
[35] P. Giannozzi, S. Baroni, N. Bonini, M. Calandra, R. Car, C. Cavazzoni, D. Ceresoli, G.L. Chiarotti, M. Cococcioni, I. Dabo, A. Dal Corso, S. de Gironcoli, S. Fabris, G. Fratesi, R. Gebauer, U. Gerstmann, C. Gougoussis, A. Kokalj, M. Lazzeri, L. Martin-Samos, N. Marzari, F. Mauri, R. Mazzarello, S. Paolini, A. Pasquarello, L. Paulatto, C. Sbraccia, S. Scandolo, G. Sclauzero, A.P. Seitsonen, A. Smogunov, P. Umari, R.M. Wentzcovitch. J. Phys.: Condens. Matter **21**, *39*, 395502 (2009).
[36] J.P. Perdew, K. Burke, M. Ernzerhof. Phys. Rev. Lett. **77**, *18*, 3865 (1996).
[37] D. Vanderbilt. Phys. Rev. B **41**, *11*, 7892(R) (1990).
[38] J. Nocedal, S.J. Wright. Numerical Optimization. In: Springer Series in Operations Research and Financial Engineering. Springer-Verlag, New York (2006). 664 p.
[39] J. Tersoff, D. Hamann. Phys. Rev. B **31**, *2*, 805 (1985).
[40] A. Otero-de-la-Roza, M.A. Blanco, A.M. Pendás, V. Luaña. Comput. Phys. Commun. **180**, *1*, 157 (2009).
[41] A. Otero-de-la-Roza, E.R. Johnson, V. Luaña. Comput. Phys. Commun. **185**, *3*, 1007 (2014).
[42] I. Horcas, R. Fernández, J.M. Gómez-Rodríguez, J. Cochero, J. Gómez-Herrero, A.M. Baro. Rev. Scient. Instrum. **78**, *1*, 013705 (2007).
[43] O.V. Yazyev, A. Pasquarello. Phys. Rev. Lett. **96**, *15*, 157601 (2006).
[44] J.E. Northrup. Phys. Rev. B **47**, *15*, 10032(R) (1993).
[45] J. Nakamura, A. Natori. Jpn. J. Appl. Phys. **44**, *7S*, 5413 (2005).
[46] Y. Yoshimoto, Y. Nakamura, H. Kawai, M. Tsukada, M. Nakayama. Phys. Rev. B **61**, *3*, 1965 (2000).
[47] L. Spiess, A.J. Freeman, P. Soukiassian. Phys. Rev. B **50**, *4*, 2249 (1994).
[48] P.E.J. Eriksson, R.I.G. Uhrberg. Phys. Rev. B **81**, *12*, 125443 (2010).
[49] K. Seino, W.G. Schmidt, F. Bechstedt. Phys. Rev. Lett. **93**, *3*, 036101 (2004).
[50] H.J.W. Zandvliet, A. van Houselt. Annu. Rev. Anal. Chem. **2**, *1*, 37 (2009).
[51] P. Borlido, T. Aull, A.W. Huran, F. Tran, M.A.L. Marques, S. Botti. J. Chem. Theory Comput. **15**, *9*, 5069 (2019).

Translated by A.Akhtyamov